ACS OMEGA

Open Access

http://pubs.acs.org/journal/acsodf

Article

Electronic Structure, Aromaticity, and Magnetism of Minimum-Sized Regular Dodecahedral Endohedral Metallofullerenes Encapsulating Rare Earth Atoms

Jia-Ming Zhang, Huai-Qian Wang,* Hui-Fang Li,* Xun-Jie Mei, Yong-Hang Zhang, and Hao Zheng

Cite This: *ACS Omega* 2024, 9, 35197−35208

Read Online

ACCESS | Metrics & More | Article Recommendations | Supporting Information

ABSTRACT: A series of minimally sized regular dodecahedron-embedded metallofullerene REC_{20} clusters (RE = Sc, Y, La, Ce, Pr, Nd, Pm, Sm, Eu, and Gd) as basic units of nanoassembled materials with tunable magnetism and UV sensitivity have been explored using density functional theory (DFT). The contribution of the 4f orbital of the rare earth atom at the center of the C_{20} cage to the frontier molecular orbital of REC_{20} gives the REC_{20} cluster additional stability. The AdNDP orbitals of the four REC_{20} superatoms that conform to the spherical jellium model indicate that through natural population analysis and spin density diagrams, we observe a monotonic increase in the magnetic moment from Ce to Gd. This is attributed to the increased number of unpaired electrons in the 4f orbitals of lanthanide rare earth atoms. The UV−visible spectrum of REC20 clusters shows strong absorption in the mid-UV and near-UV bands. REC_{20} clusters encapsulating lanthanide rare earth atoms stand out for their tunable magnetism, UV sensitivity, and stability, making them potential new self-assembly materials.

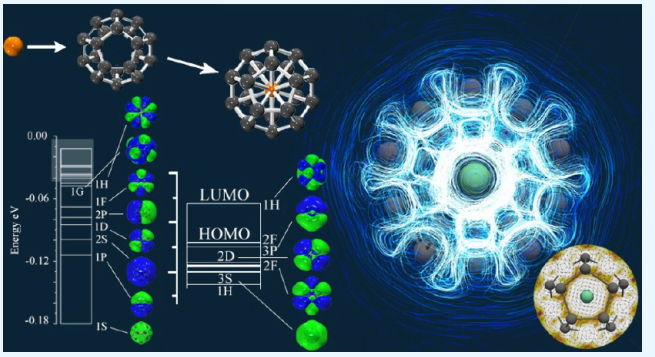

1. INTRODUCTION

Since embedded metallofullerene has metal atoms embedded inside the fullerene cavity, its growth and stabilization mechanism are more complex and are still an unsolved mystery. Fullerene superatoms can serve as special building blocks for constructing nanomaterials due to their ability to encapsulate atoms or molecules.[1−5] In 1985, Heath et al. discovered the first stable embedded metal complex, LaC_{60}, which was named metallofullerene.[6] Since then, a rich variety of endohedral metallofullerenes (EMFs) with different cage sizes and embedded atoms have been extensively studied.[7−19] Compared to larger-sized fullerenes, small fullerenes are relatively unstable due to increased curvature, causing strain within the cage and weakening π-conjugation.[20−22] Especially for the smallest fullerene C_{20}, which has all pentagonal faces, the bonds tend to be sp^3 bonds rather than the sp^2 bonds that are dominant in large fullerenes.[16] Through metal doping, it is possible to increase the stability of smaller fullerenes and change their electronic properties.[23−35] T. Guo et al.[23] reported in 1992 that the experiment of MC_{28} confirmed that the 5f feature of U in the photoemission spectra of UC_{28} existing in sublimed films is consistent with the formal 4^+ valence state of U. Later, Dunk et al.[28] used FT-ICR (Fourier transform ion cyclotron resonance) mass spectrometry and found relatively high abundance of MC_{28} cations encapsulating group 4 metal atoms and U. The success of the experiment inspired a large number of *ab initio* reports on small-sized EMFs. A series of EMFs MC_{28} (M = Ti, Zr, Hf, U),[34,35] UC_{26},[29] and PuC_{24}[31] of various sizes with large HOMO−LUMO gaps that meet the characteristics of 32-electron systems have been widely reported.

Among all small-sized embedded metallofullerenes, MC_{20} has also attracted a great deal of attention as the smallest-sized encapsulation material. Many *ab initio* calculations have been performed for the smallest sized EMFs using a variety of doping atoms that significantly change their stability, electronic structure, and magnetic properties.[36−47] Manna and Ghanty reported $M@C_{20}$ (M = Pr^-, Pa^-, Nd, U, Pm^+, Np^+, Sm^{2+}, Pu^{2+}, Eu^{3+}, Am^{3+}, Gd^{4+}, and Cm^{4+}), which exhibit special stability with 26 electrons (HOMO−LUMO energy gap in the range of 2.5−4.9 eV).[42] These valence electrons correspond to the fully occupied spd-type energy levels of the cage and the partially occupied f-type molecular orbitals of the cage. In addition, F. Meng et al. designed a series of 32-electron systems consistent with shell closing and obtained MC_{20} with a larger HOMO−

Received: June 25, 2024
Revised: July 19, 2024
Accepted: July 23, 2024
Published: August 2, 2024

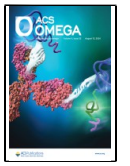

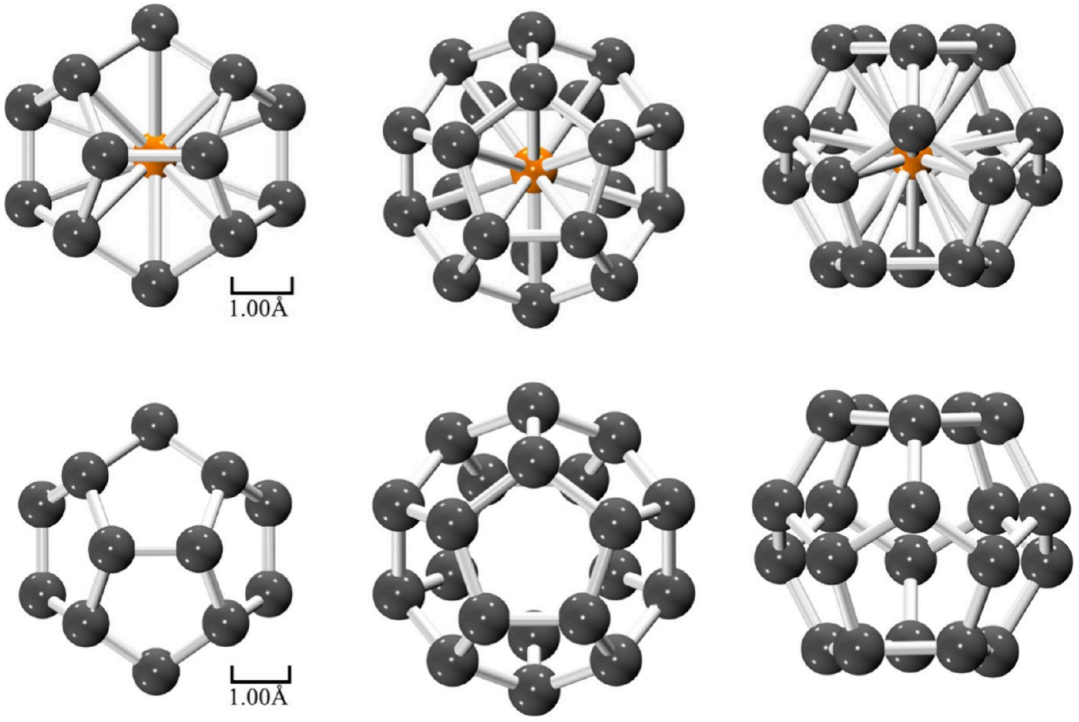

Figure 1. Structure images from three different viewing angles of REC_{20} clusters (RE = Sc, Y, La, Ce, Pr, Nd, Pm, Sm, Eu, Gd) optimized at the PBE0/RE/SDD//C/cc-pVTZ level and the structure of the C_{20} cluster at the PBE0/C/cc-pVTZ level. The orange balls and gray balls represent RE atoms and C atoms, respectively.

LUMO energy gap (2.22−5.39 eV), where M = Eu^{3-}, Am^{3-}, Gd^{2-}, Cm^{2-}, Tb^{-}, Bk^{-}, Dy, Cf, Ho^{+}, Es^{+}, Er^{2+}, Fm^{2+}, Tm^{3+}, Md^{3+}, Yb^{4+}, No^{4+}, Lu^{5+}, and Lr^{5+}.[44]

Previous reports on EMFs have tended to incorporate metal atoms that enable them to meet a specific number of valence electrons to exhibit special stability. This article focuses on rare earth (RE) elements, trying to find EMFs with special stability outside of these rules and exploring the effects of encapsulating different RE atoms on the structure, electronic properties, magnetism, and aromaticity of REC_{20} (RE = Sc, Y, La, Ce, Pr, Nd, Pm, Sm, Eu, Gd). The main purposes of this study are (1) to obtain the geometric structure and energy properties of a series of REC_{20} clusters and (2) to explore the effects of encapsulating different rare earth elements on the electronic distribution and magnetism of REC_{20} clusters. (3) The analysis of the electronic structure of REC_{20} clusters provides valuable theoretical guidance for researchers to develop cluster-assembled nanomaterials with special magnetic properties.

2. THEORETICAL METHOD AND COMPUTATIONAL DETAILS

The structures of a series of minimally EMFs encapsulating rare earth atom REC_{20} clusters (RE = Sc, Y, La, Ce, Pr, Nd, Pm, Sm, Eu, and Gd) have been optimized using density functional theory (DFT). DFT calculations use the PBE0[48] functional, which has successfully predicted the structure of silicon-based and germanium-based clusters doped with lanthanide rare earth atoms of various sizes.[49−51] The optimization of the structures of REC_{20} clusters has been divided into two steps. The larger scalar Stuttgart relativistic effective core potential basis set (ECP10MDF[52] for Sc; ECP28MWB[53] for Y; ECP46MWB[54,55] for La; ECP48MWB for Ce and Pr; ECP50MWB for Nd and Pm; ECP52MWB for Sm and Eu; ECP54MWB for Gd) is chosen for rare earth atoms, and the 6-31g(d,p)[56,57] basis set was selected for C during the first optimized process. The cluster structure obtained in the first step is then optimized again at the higher computational level PBE0/RE/SDD//C/cc-pVTZ[52,53,58,59] to obtain more accurate structural and energy information. To ensure that the energy minimum was achieved, various probable spin multiplicities were considered, and the harmonic vibrational frequencies were also calculated to guarantee that the optimized structures represented local minima. All optimization calculations were performed by the Gaussian09 program.[60]

All kinds of wave function analyses, including atomic dipole corrected Hirshfeld atomic charge (ADCH), the spin density ($\rho_{alpha} - \rho_{beta}$) isosurface, and iso-chemical shielding surfaces (ICSS),[61−63] were conducted by the multifunctional wave function (Multiwfn) analyzer program,[64] visualized by VMD[65] and ParaView[66] software. Gauge-including magnetically induced current (GIMIC) is generated by the GIMIC2.0[67] and Gaussian09 programs.[60]

3. RESULTS AND DISCUSSION

3.1. Geometric Structure and HOMO−LUMO Gap. The schematic representation of the structures of REC_{20} clusters (RE = Sc, Y, La, Ce, Pr, Nd, Pm, Sm, Eu, and Gd) optimized at the PBE0/RE/SDD//C/cc-pVTZ level is portrayed in Figure 1. Specific structural details are listed in Figure S1. To ensure consistency of the results, we optimized the structure of the C_{20} cluster under the PBE0/C/cc-pVTZ computational model. The energy of caged C_{20} with C_{2h} symmetry is consistent with the results previously reported by Zeng[68] at the same computational level. Table S1 gives the atomic coordinates of the C_{20} and REC_{20} clusters. The RE atoms of the REC_{20} cluster are all located in the center of REC_{20}. The C−C bond length in all REC_{20} clusters is between 1.44 and 1.55 Å. It can

https://doi.org/10.1021/acsomega.4c05912
ACS Omega 2024, 9, 35197−35208

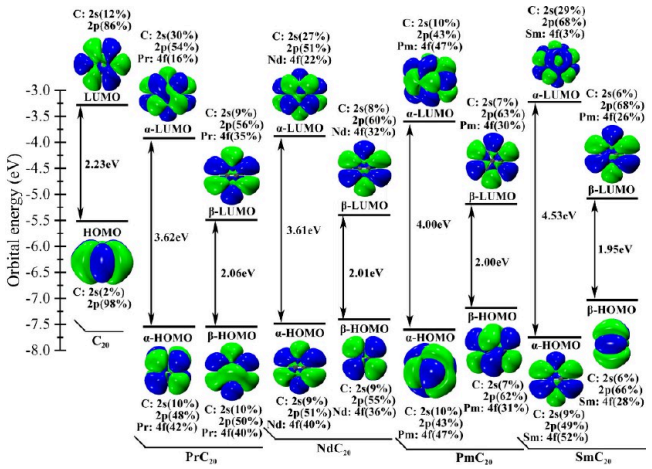

Figure 2. HOMO−LUMO gaps (indicated in black) in conjunction with corresponding orbitals (isosurfaces = 0.002) of REC_{20} (RE = Pr, Nd, Pm, and Sm) are obtained at the PBE0/RE/SDD//C/cc-pVTZ level, and C_{20} is obtained at the C/cc-pVTZ level.

Table 1. Ionization Potential (IP), Electron Affinity (EA), and Chemical Hardness (η) of REC_{20} and C_{20} Clusters at the PBE0/RE/SDD//C/cc-pVTZ Level

Cluster	IP (eV)	EA (eV)	η (eV)
C_{20}	7.06	1.79	2.63
ScC_{20}	7.35	2.53	2.41
YC_{20}	7.85	2.92	2.46
LaC_{20}	8.05	3.47	2.29
CeC_{20}	8.56	3.81	2.38
PrC_{20}	8.79	2.48	3.15
NdC_{20}	8.75	2.97	2.89
PmC_{20}	8.54	3.52	2.51
SmC_{20}	9.27	3.82	2.73
EuC_{20}	7.22	2.23	2.50
GdC_{20}	7.31	2.52	2.40

be seen that the encapsulated RE atoms have little impact on the original structure of C_{20}. Among them, EuC_{20} has the highest T_h symmetry, CeC_{20} and PmC_{20} clusters show D_{3d} symmetry, LaC_{20} has D_{2h} symmetry, and the other REC_{20} clusters (RE = Sc, Y, Pr, Nd, Sm, and Gd) show the symmetry of C_i. It can be seen that embedding different RE atoms can change the symmetry of the C_{20} cage.

The HOMO−LUMO gaps and molecular orbital compositions of REC_{20} (RE = Pr, Nd, Pm, and Sm) clusters obtained by NAO analysis are plotted in Figure 2. Simultaneously, we calculated the ionization potential (IP), electron affinity (EA), and the chemical hardness (η) of the REC_{20} clusters using the following formula as a more accurate measure of their chemical stability,[69] with the results presented in Table 1.

$$\eta = (\mathrm{IP} - \mathrm{EA})/2 \quad (1)$$

The molecular orbital compositions of all REC_{20} clusters are plotted in Figure S2 and Figure S3. For ScC_{20} and YC_{20} clusters encapsulating Sc atoms in the fourth period and Y atoms in the fifth period, their central atoms make little contribution to the frontier orbital. This implies that the electronic structures of Sc and Y atoms may not directly affect the reactivity of ScC_{20} and YC_{20} clusters. For the REC_{20} clusters encapsulating lanthanide atoms, the contribution of RE atoms to the frontier orbitals mainly comes from the 4f orbital. Interestingly, for several of the REC_{20} clusters (RE = Pr, Nd, Pm, Sm), the RE atoms make a significant contribution to the 4f electrons of the α-HOMO orbital, among which Pr, Nd, Pm, and Sm contribute significantly to the α-HOMO orbital. The contribution values are 42%, 40%, 47%, and 52%, respectively. At the same time, these REC_{20} clusters have large HOMO−LUMO gaps exceeding 3.5 eV, which means that these clusters can be regarded as stable superatoms.[12,16] The HOMO−LUMO gaps and η reflect the ability of electrons to jump from occupied orbitals to unoccupied orbitals, which means they have higher chemical stability.[40,70,71] Overall, the greater the contribution of the 4f orbital of the RE atom located in the center of the C_{20} cage to the α-HOMO orbital, the larger the corresponding HOMO−LUMO gap, which means that the 4f orbital of the RE atom has an important contribution to the chemical stability of REC_{20}.

3.2. Spherical Jellium Model. Four REC_{20} (RE = Pr, Nd, Pm, Sm) clusters with larger η that exhibit special chemical stability are potentially stable superatoms. Their electronic arrangement analysis results show that the electronic arrangement of REC_{20} is fully consistent with the spherical jellium model (SJM). In the SJM model, when the number of valence electrons in the cluster is 2, 8, 18, 20, 34, ..., each shell can be filled, and it can be written as $1S^2$, $2P^6$, $1D^{10}$, $1F^{14}$, $2S^2$, ...[72] The valence molecular orbital of the REC_{20} cluster is shown in Figure 3. In addition, the complete molecular orbital of the REC_{20} cluster is shown in Supporting Information Figure S4.

Each carbon atom is bonded to the adjacent carbon atom through sp^2 hybridization, and the p_z electrons of the C atom are left to provide valence electrons for the superatom. In Figure 3, except for the 1H shell orbital, the remaining superatomic orbitals are formed by hybridization of the p_z electrons of the carbon atom and the RE atom. The $1H^{18}$ orbitals with higher angular momentum of all REC_{20} superatoms are split into two parts, the preferentially occupied $1H^{10}$ orbitals and the LUMO orbital. As shown in Figure 3, encapsulating different RE atoms will affect the energy distributions of the 1P shell and the 1F shell. For PmC_{20} and SmC_{20} with higher spins, their 1F shells are clearly split into two parts, single electron occupied (blue line) orbitals and fully occupied orbitals with lower energy than 1P shell electrons. SmC_{20}, which has the highest spin multiplicity, has energy degeneracy in its fully occupied 1F shell orbitals and lower energy 1D shell orbitals. Except for the 1F shell, the electron distribution of all superatomic orbitals in which p_z electrons of carbon atoms participate in hybridization can be written as $1S^2$, $1D^{10}$, and $1P^6$. It satisfies the $2(N + 1)^2$ rule proposed by Hirsch et al. ($N = 2$).[73]

For the four REC_{20} (RE = Pr, Nd, Pm, and Sm) clusters, their HOMO orbitals and LUMO orbitals belong to different shells. Since the energy difference between electron orbitals with different angular momentum is large, they exhibit a large HOMO−LUMO gap.

3.3. Magnetic Moment and Electron Spin Density. In order to further investigate the influence of RE atoms on C_{20}, the natural population analysis (NPA)[74] and ADCH atomic charge[75] of REC_{20} clusters were calculated to explore the charge transfer and charge distribution characteristics of REC_{20} clusters. The natural electron configuration (NEC), natural charge population (NCP), Hirshfeld charge, and ADCH charges of RE atoms are shown in Table 2.

NPA indicates that the charge of the inner orbital (4s, 5s, and 6s) of all RE atoms is transferred to the outer orbital. For

https://doi.org/10.1021/acsomega.4c05912
ACS Omega 2024, 9, 35197−35208

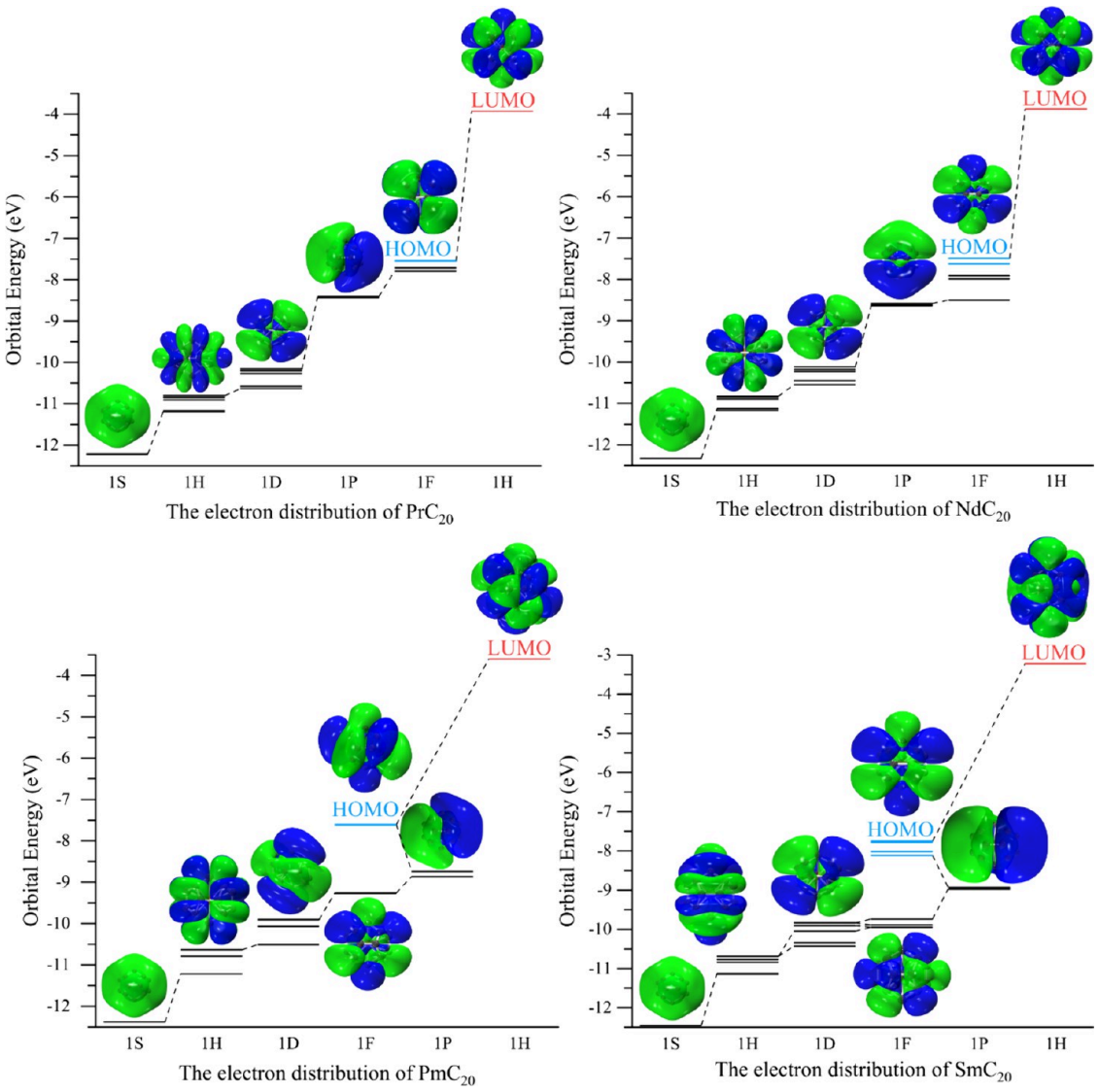

Figure 3. Valence molecular orbitals of REC_{20} (RE = Pr, Nd, Pm, Sm) clusters. The blue lines represent single electron occupied orbitals, and the red lines represent LUMO orbitals.

the Sc atom, charges are mainly transferred to the outer 3d and 4p orbital. The difference is that the Y atom charges are mainly transferred to the 5p and 5d orbitals with higher energy. For lanthanide atoms (La, Ce, Pr, Nd, Pm, and Sm) whose 4f orbital is not half full, the charge is more likely to be transferred to the 4f orbital, and the charge distribution of the 5d orbital is always around 2.5. As the 4f electron layer gradually reaches half full, the NCP of the lanthanide atoms gradually increases, and the charge transferred from the C_{20} cage to the RE atom gradually decreases. Except for the Y atom, the NCP and ADCH charges of the other RE atoms are negative and behave as charge acceptors. This is because the RE atom is located at the central charge accumulation position within C_{20}. The completely opposite charge transfer properties shown by NCP and ADCH charges about the Y atom may be due to the vagueness of the minimum set/Rydberg set division criteria of these elements when calculating the NPA charges of transition metal elements, and different divisions will affect the occupancy number as a weighted symmetry orthogonalization (OWSO) process, which in turn affects the charge value.[76] Compared with NEC, ADCH charges of RE atoms show better consistency.

Table 3 lists the calculated local magnetic moments of the 6s, 4f, 5d, 5f, and 6d orbitals of RE (RE = La, Pr, Nd, Pm, Sm, Eu) atoms and the total magnetic moments of the REC_{20} clusters. As shown in Table 3, the magnetic moments of REC_{20} mainly come from the contribution of unpaired electrons in the 4f orbital of RE atoms. Transferred to the 6p orbital, the electrons in the orbital do not contribute to the magnetic moment, and the contributions of the 5d, 6d, and 7s orbitals are very small and almost negligible. The GdC_{20} cluster has the largest total magnetic moment (6 μ_B) among the REC_{20} clusters. This also shows that the 5d orbital electrons of RE atoms participate in bonding with the C_{20} cage. In addition, since the La atom has very few unpaired electrons in the 4f orbital, it does not exhibit an obvious magnetic moment. It is worth noting that the magnetic moments on RE (RE = Pm, Sm, and Eu) atoms are even larger than total magnetic moments, indicating that the contribution of C to the total magnetic moment is very limited.

https://doi.org/10.1021/acsomega.4c05912
ACS Omega 2024, 9, 35197−35208

Table 2. Natural Electron Configuration (NEC), Natural Charge Population (NCP), and ADCH Charge of RE (RE = Sc, Y, La, Ce, Pr, Nd, Pm, Sm, Eu, Gd) Atoms in REC_{20} Clusters

	NPA		
Cluster	NEC	NCP of RE (e)	ADCH charges of RE (e)
ScC_{20}	[core]$4s^{0.30}3d^{3.53}4p^{1.00}4d^{0.37}$	−2.19	−0.61
YC_{20}	[core]$5s^{0.33}4d^{1.05}5p^{0.71}6s^{0.01}5d^{0.42}$	0.51	−0.63
LaC_{20}	[core] $6s^{0.30}4f^{4.25}5d^{2.09}6p^{0.86}5f^{0.07}6d^{0.28}7p^{0.01}$	−4.70	−0.67
CeC_{20}	[core] $6s^{0.31}4f^{4.50}5d^{2.47}6p^{0.89}5f^{0.16}6d^{0.35}7p^{0.02}$	−4.66	−0.59
PrC_{20}	[core] $6s^{0.32}4f^{5.17}5d^{2.40}6p^{0.89}5f^{0.23}6d^{0.39}7p^{0.02}$	−4.39	−0.46
NdC_{20}	[core] $6s^{0.33}4f^{5.69}5d^{2.49}6p^{0.89}5f^{0.47}6d^{0.38}7p^{0.02}$	−4.23	−0.49
PmC_{20}	[core] $6s^{0.33}4f^{6.15}5d^{2.58}6p^{0.91}5f^{0.60}6d^{0.35}7p^{0.02}$	−3.90	−0.50
SmC_{20}	[core] $6s^{0.34}4f^{7.01}5d^{2.59}6p^{0.91}5f^{0.56}6d^{0.34}7p^{0.01}$	−3.73	−0.53
EuC_{20}	[core] $6s^{0.34}4f^{7.48}5d^{2.44}6p^{0.92}5f^{0.43}6d^{0.34}7p^{0.01}$	−2.93	−0.51
GdC_{20}	[core] $6s^{0.36}4f^{7.78}5d^{2.40}6p^{0.92}7s^{0.12}5f^{0.36}6d^{0.36}$	−2.24	−0.65

In order to visualize the distribution of single electrons in three-dimensional space, the spin density ($\rho_{alpha} - \rho_{beta}$) isosurface of REC_{20} (RE = Sc, Y, La, Pr, Nd, Pm, Sm, Eu) is shown in Figure 4. In the closed-shell system of CeC_{20}, there is no spin density. The Figure 4 clearly shows that in the three systems of ScC_{20}, YC_{20}, and LaC_{20} clusters, which have almost no magnetic moments, the unpaired electrons are mainly distributed on the outer C_{20} cage. There is no spin electron distribution around the SC and Y atoms in the cage, and only a very small amount of spin electrons is distributed on the La atom in the C_{20} cage. Although the spin density isosurface of the C_{20} cage surface expands as the incorporated Sc, Y, and La atomic numbers increase, the increase in spin electrons on the C_{20} cage does not contribute to the total magnetic moments of the system. Starting from PrC_{20}, the green area gathers from the C_{20} cage to the central atom, showing two sets of intersecting cross shapes. Among them, PmC_{20} is special. Spin electrons are densely distributed around the Pm atom in the cage (green area), and the number of spin electrons distributed on the C_{20} cage is very small. This can also explain the phenomenon that the magnetic moment on the Pm atom is greater than the total magnetic moment. As the RE doping element changes, we can observe that the green isosurfaces inside and outside the cage gradually expand. Based on the

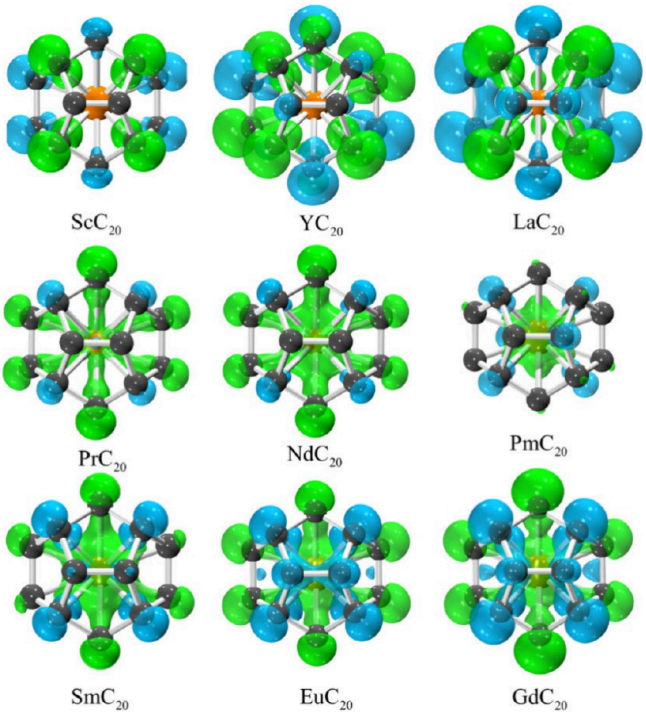

Figure 4. Spin-density ($\rho_{alpha}-\rho_{beta}$) isosurfaces of REC_{20} (RE = Sc, Y, La, Ce, Pr, Nd, Pm, Sm, Eu, and Gd). The isosurface is set to ±0.005. The green and blue isosurfaces show that the spin density has positive and negative values, respectively. Orange and gray balls represent RE atoms and carbon atoms, respectively.

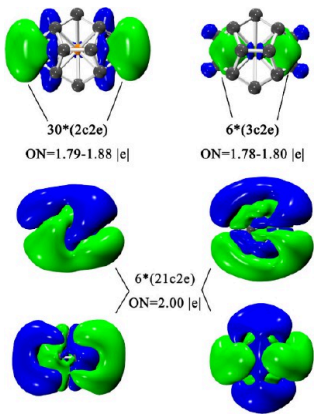

Figure 5. Bonding analyses of the AdNDP orbitals of PrC_{20}. The occupation numbers (ONs) are indicated.

Table 3. Magnetic Moments (μ_B) of the 6s, 4f, 5d, 5f, 7s, and 6d Orbitals of RE Atoms (RE = La, Pr, Nd, Pm, Sm, Eu, Gd), the Total Magnetic Moments of the RE Atoms, and the Total Magnetic Moments of the Most Stable Isomers

	Magnetic moments of RE atoms (μ_B)							
Cluster	6s	4f	5d	7s	5f	6d	RE	Total
LaC_{20}	0.00	0.03	−0.01	0.00	0.13	0.00	0.15	1
PrC_{20}	0.00	0.45	0.00	0.00	0.03	0.00	0.48	1
NdC_{20}	0.00	1.25	0.00	0.00	0.14	0.01	1.40	2
PmC_{20}	0.00	2.83	0.02	0.00	0.30	0.03	3.18	3
SmC_{20}	0.00	3.87	0.02	0.00	0.19	0.02	4.1	4
EuC_{20}	0.00	5.20	0.02	0.00	0.17	0.04	5.43	5
GdC_{20}	0.07	5.80	0.02	−0.17	0.10	0.04	5.86	6

https://doi.org/10.1021/acsomega.4c05912
ACS Omega 2024, 9, 35197−35208

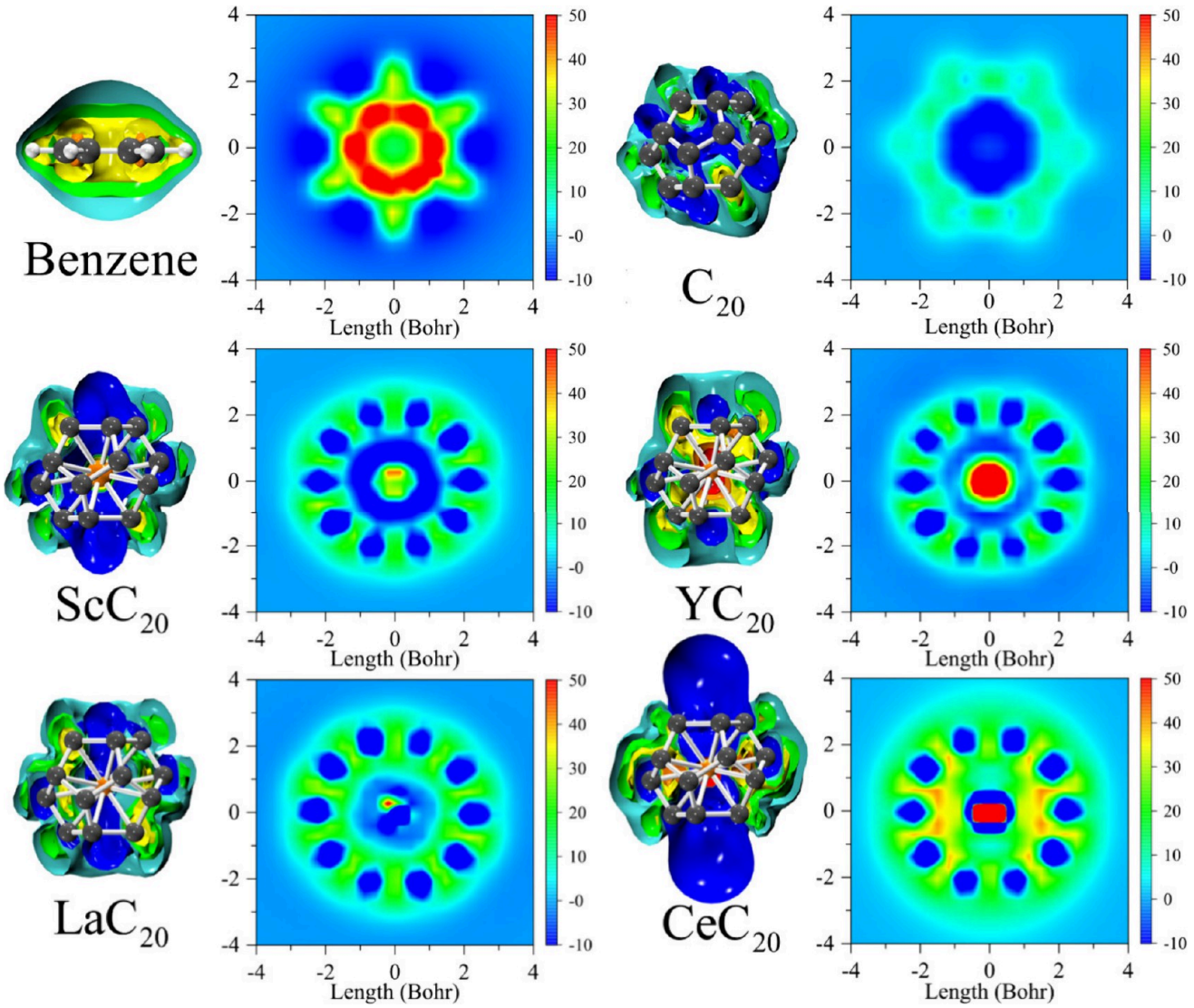

Figure 6. ICSSzz of benzene, C_{20}, and REC_{20} (RE = Sc, Y, La, Ce) The color-filled maps are the ICSSzz distribution at the plane of the RE atom. Each contour shows the corresponding shielding surface separately, cyan at 4 ppm, green at 8 ppm, yellow at 16 ppm, orange at 32 ppm, red at 64 ppm, and blue at −4 ppm, respectively.

above phenomenon, the magnetic moments of the REC_{20} clusters mainly come from the contribution of unpaired electrons around the RE atoms in the C_{20} cage, and the spin electrons on the C_{20} cage have a limited contribution to the total magnetic moment. When the number of spin electrons in the C_{20} cage is greater than the number of spin electrons on the C_{20} cage, the total magnetic moment on the RE atom exceeds the total magnetic moment of the system.

Based on the above conclusion, REC_{20} clusters doped with lanthanide RE atoms are mainly bonded through the 5d orbital of RE, while the 4f electrons hardly participate in bonding. Combined with magnetic moment analysis, most 4f electrons are not bonded between RE atoms and C_{20} cages, which means that almost all unpaired electrons remain in this orbital, resulting in an adjustable magnetic spin magnetic moment. It is the tunable magnetic moment exhibited by REC_{20} clusters that gives them the potential to become the basic structure of new magnetic nanoassembly materials.

3.4. AdNDP. To further investigate the electronic properties of the four REC_{20} (RE = Pr, Nd, Pm, and Sm) clusters that exhibited higher stability, the electronic interactions between neighboring atoms within the REC_{20} clusters were studied by adaptive natural density partitioning (AdNDP).[77]

Taking PrC_{20} as an example, its AdNDP orbital is shown in Figure 5, and the AdNDP orbitals of the other three clusters are shown in Figure S5. In all four REC_{20} clusters, excluding the electrons that contribute to the magnetic moment, there are 42 pairs of electrons that can be divided into three types. First, there are 30 2c-2e localized σ C−C bonds on the surface of the C_{20} cage, and their occupation numbers (ON) are between 1.79 and 1.88|e|. Second, there are 6 delocalized 3c-2e σ bonds with ON between 1.78 and 1.80 in its cage, which form a triangular area on the inside of the cage. This indicates that the encapsulation of Pr atoms enhances the stability of the C_{20} cage. The shapes of all 2c-2e and 3c-2e orbitals are similar to those shown in Figure 5. Finally, the 6 fully delocalized 21c-2e orbitals present the four configurations shown in Figure 5, which roughly present shapes similar to those of the P shell and D shell electron orbitals. The six 21c-2e pi bonds with ON = 2.00|e| indicate that the delocalized electrons are not only present on the surface of the C_{20} cage but also distributed inside it. The delocalized electrons distributed inside the cage

https://doi.org/10.1021/acsomega.4c05912
ACS Omega 2024, 9, 35197−35208

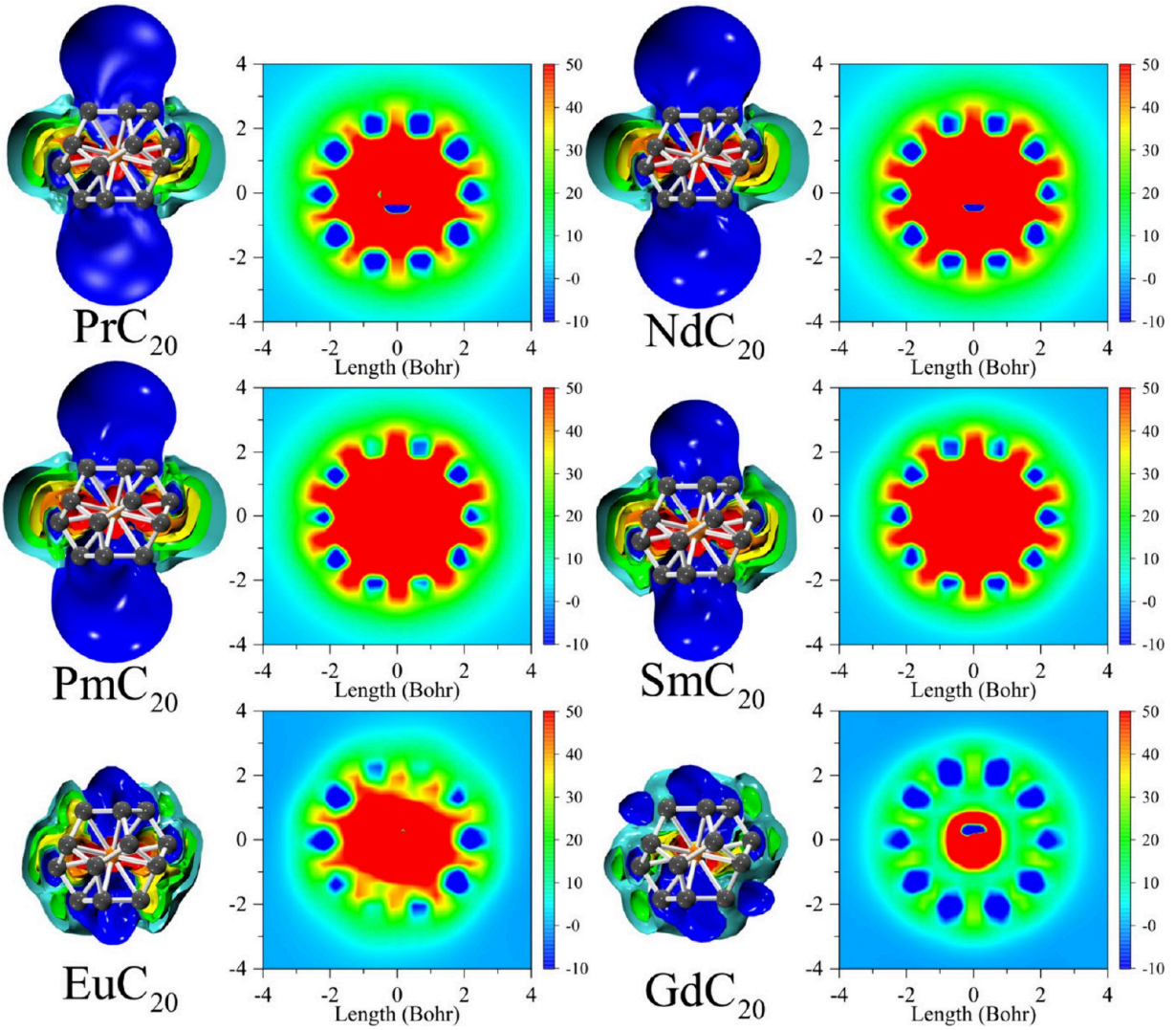

Figure 7. ICSSzz of REC_{20} (RE = Pr, Nd, Pm, Sm, Eu, or Gd). The color-filled maps are the ICSSzz distribution in the plane of the RE atom. Each contour shows the corresponding shielding surface separately, cyan at 4 ppm, green at 8 ppm, yellow at 16 ppm, orange at 32 ppm, red at 64 ppm, and blue at −4 ppm, respectively.

of the REC_{20} cluster indicate that it has a certain degree of aromaticity.

3.5. Aromaticity. It can be seen from the spin density isosurface that there are delocalized electrons between RE atoms and the C_{20} cage, which make the REC_{20} cluster have a certain degree of aromaticity. The impact of encapsulating different RE atoms on the aromaticity of REC_{20} clusters was further explored by calculating the ICSS of REC_{20} clusters.[62,78] ICSS corresponds to the original definition of nucleus-independent chemical shift (NICS), which embodies isotropic shielding against external magnetic fields.[61,62] Based on NICS, ICSS not only considers the shielding value of a specific point but considers the magnetic shielding value as a real space function and studies it by drawing curve diagrams, plane diagrams, and isosurface diagrams to obtain more comprehensive information. The symbol definitions of ICSS and NICS are exactly the opposite. NICS takes the negative value of the magnetic shielding value, while ICSS directly displays the magnetic shielding value at different locations without taking the negative sign. In other words, the more positive the ICSS is, the greater the degree of shielding from the external magnetic field at this point. The more negative the ICSS is, the stronger the degree of deshielding at this location. We calculated the isosurface of the ZZ component of the cluster ICSS (ICSSzz[63,79]) of REC_{20} clusters, where the Z direction is perpendicular to the five-atom ring in C_{20}. Figure 6 shows the color-filled maps of ICSSzz at the plane of the RE atom in REC_{20}. The three-dimensional cluster magnetic shielding isosurface of ICSSzz was also plotted for a comparison of color-filled maps. In addition, the ICSSzz of benzene and C_{20} are shown in Figure 6 for comparison.

The ICSSzz value at the center of C_{20} in Figure 6 is negative, which means that there is a deshielding region at the center of C_{20}, which is consistent with the positive NICS value at the center of C_{20} in previous reports.[80] The ICSSzz isosurface distribution of REC_{20} clusters shown in Figure 6 and Figure 7 reveals that the aromaticity of C_{20} cages encapsulating different RE atoms is very different. For non-lanthanide elements, the REC_{20} clusters encapsulated by Sc atoms and Y atoms show antiaromatic properties as a whole (blue area). This is due to the limited number of electrons in the Sc atoms and Y atoms themselves and their inability to provide delocalized electrons in the cage. In the LaC_{20} cluster encapsulating La, the first element of the lanthanide series, the ICSSzz value around the

https://doi.org/10.1021/acsomega.4c05912
ACS Omega 2024, 9, 35197−35208

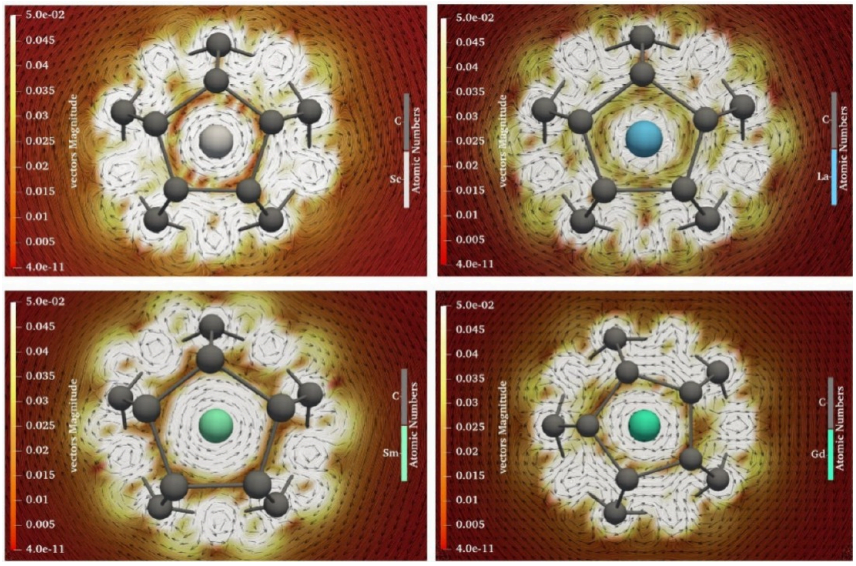

Figure 8. GIMIC maps of REC_{20} (RE = Sc, La, Sm, and Gd) clusters on the central plane with the magnetic field direction forward along the *z*-axis (the perpendicular plane facing outward).

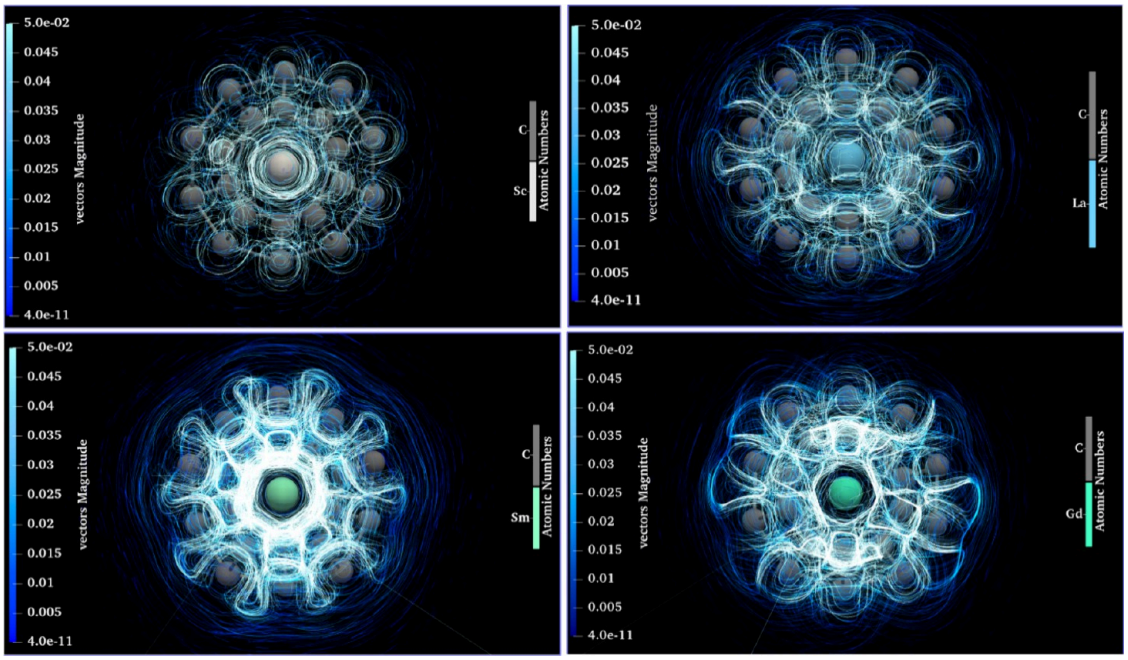

Figure 9. Screenshots of the GIMIC for REC_{20} (RE = Sc, La, Sm, and Gd) clusters.

central atom is almost 0. The interior of the LaC_{20} cage can be considered as a deshielding region. As the atomic number increases, a ring-shaped strong magnetic shielding region appears in the central plane of the REC_{20} cluster. The overall isosurface is distributed in a spindle shape, showing an extremely strong magnetic shielding region (red area) in the central plane inside the cage, while a huge deshielding region appears along the *z*-axis outside the C_{20} cage. This reveals that the limited delocalized distribution of free electrons in the 4f orbital of lanthanide atoms of the REC_{20} cluster forms a ring-shaped magnetic shielding region. However, for the EuC_{20} and GdC_{20} clusters that exhibit the highest magnetic moments, the aromaticity at the central plane does not continue to strengthen but weakens, which is likely due to the delocalization of free electrons in a larger area within the cage. The antiaromatic areas on the outside of the EuC_{20} and GdC_{20} cages are significantly suppressed, and the aromatic ring width increases significantly, almost covering the entire side of the C_{20} cage. This may also reflect that the magnetic shielding region of the cluster is no longer highly concentrated near the central atom but is strengthened overall. This all implies that the delocalized electrons are distributed over a larger area within the cage.

From the above discussion, it can be concluded that the aromaticity of REC_{20} clusters encapsulating different RE atoms is affected by the distribution of delocalized electrons within the cage. When there are fewer delocalized electrons, the REC_{20} cluster cage is a deshielding region. As the RE atomic number increases, the number of delocalized electrons further increases. The transformation of the ICSSzz isosurface from a

https://doi.org/10.1021/acsomega.4c05912
ACS Omega 2024, 9, 35197−35208

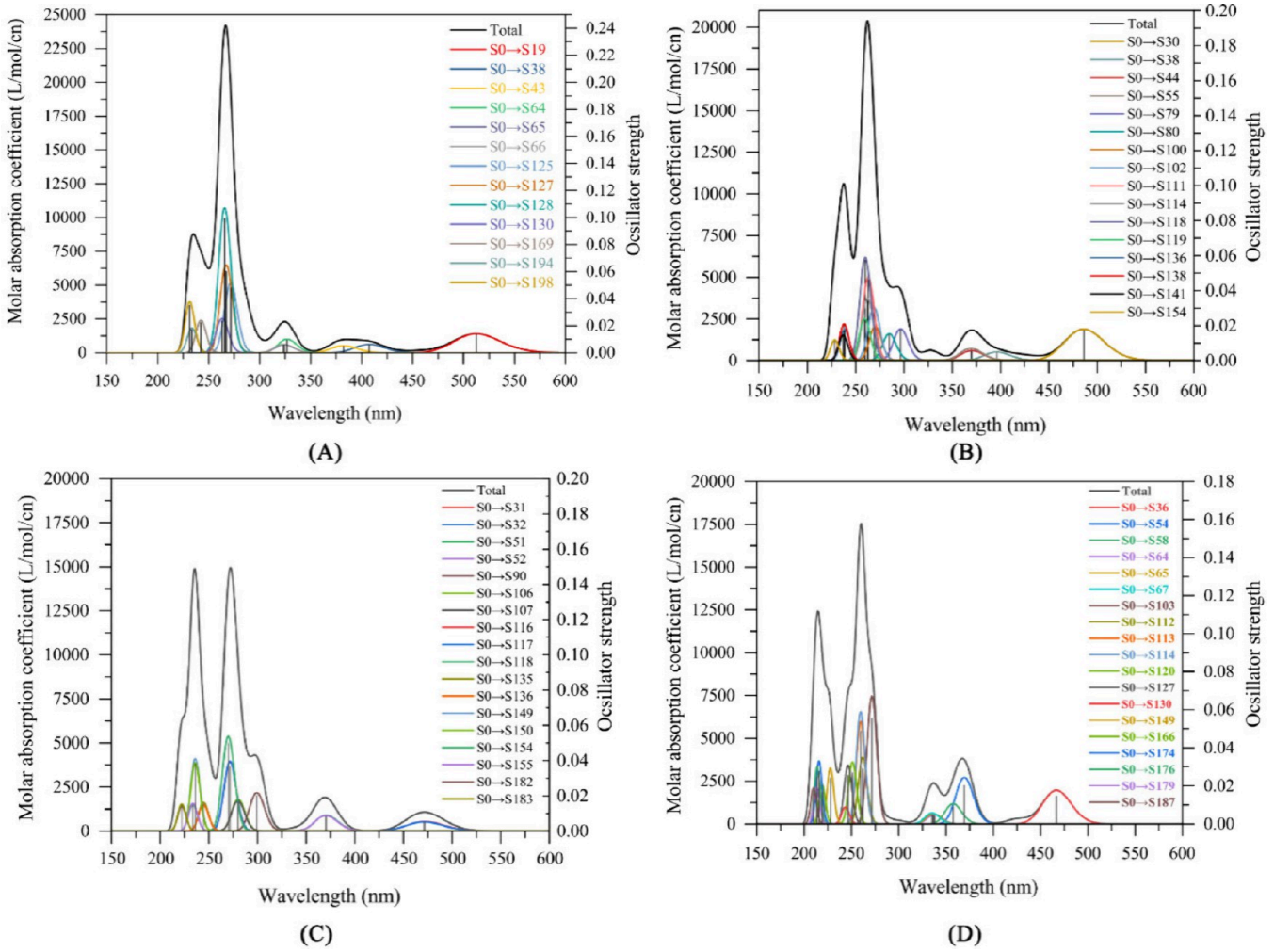

Figure 10. Calculated UV−vis spectra of REC_{20} (RE = Pr, Nd, Pm, Sm) clusters. Curves and vertical lines represent the absorption spectra and oscillator strength, respectively. (a) PrC_{20}, (b) NdC_{20}, (c) PmC_{20}, and (d) SmC_{20}.

local narrow ring to a hemispherical shape wrapping the sides of the C_{20} cage implies that the delocalized electron distribution trend in the cage is from concentrated distribution in the central part to uniform distribution within the cage.

3.6. Molecular Magnetically Induced Current. In order to more intuitively observe the effect of encapsulating different RE atoms on the aromaticity of REC_{20} clusters, the molecular magnetically induced current of REC_{20} clusters was calculated using the GIMIC program package.[67] The GIMIC program implements the gauge-including magnetically induced current method. The GIMIC method is based on gauge-including/invariant atomic orbitals (GIAO) and relies on the density matrix produced by the magnetic properties calculation process and the derivative matrix of the density matrix with respect to the magnetic field to calculate the induced current density.[67,81] Several representative REC_{20} clusters (RE = Sc, La, Sm, Gd) were selected, and the plane-shaded streamline diagrams and arrow diagrams of the modes of the magnetically induced current at their central plane are shown in Figure 8. A three-dimensional dynamic visual representation of the magnetically induced current is provided in the Supporting Information, and Figure 9 shows some screenshots.

In Figure 8, the ScC_{20} clusters have obvious paramagnetic currents in the regions around the Sc atoms due to the presence of deshielding regions inside the ScC_{20} clusters. In contrast, in SmC_{20} clusters with a strong magnetic shielding region in the central plane, the strong diamagnetic current formed within the SmC_{20} cage appears as a large circular white area bright near the Sm atoms. Compared with SmC_{20}, although diamagnetic current is also generated near the central atom of LaC_{20}, due to the deshielding area inside it, the diamagnetic current intensity is very weak, and the distribution is unevenly elliptical. It is worth noting that the diamagnetic current within the cage of the GdC_{20} cluster is obviously distributed over a larger area, which is obviously caused by the distribution of delocalized electrons in a larger area. Although both the paramagnetic current and diamagnetic current appear near the central atom simultaneously, overall the GdC_{20} cluster still shows strong aromaticity.

3.7. UV−Vis Spectra. In order to further understand the optical properties of the four REC_{20} (RE = Pr, Nd, Pm, and Sm) clusters with high stability, UV−vis spectra were simulated by calculating the time-dependent density functional theory (TD-DFT) at the PBE0/RE/SDD//C/cc-pVTZ level. In order to ensure the accuracy of the calculation, it is necessary to consider enough energy bands, and 200 excited states were found in the REC_{20} clusters.

The four REC_{20} clusters all show five absorption bands, one of which is located in the visible light part and the other four are located in the near-ultraviolet region and the mid-

https://doi.org/10.1021/acsomega.4c05912
ACS Omega 2024, 9, 35197−35208

ultraviolet region. The highest peak position of each absorption band is marked in Figure 10. The UV−vis spectra of the four REC_{20} clusters show that their main absorption regions are all located in the mid-ultraviolet band, accounting for 87.54% (PrC_{20}), 90.47% (NdC_{20}), 91.92% (PmC_{20}), and 79.56% (SmC_{20}) of the total, respectively. The encapsulation of different RE atoms mainly affects the intensity of the first absorption band, among which the first absorption band of the PmC_{20} cluster is the strongest. The second absorption band located in the mid-ultraviolet region is almost unaffected by the RE atoms, which is mainly due to its characteristics of the C_{20} cage $\pi \rightarrow \pi^*$ electronic transition. The ADCH charge of the RE atom indicates that the embedded RE atom causes electron transfer from the C_{20} cage to the RE atom, resulting in a blue shift in the UV−vis spectrum of the REC_{20} cluster with an increasing atomic number of the encapsulated RE. In summary, the UV−visible spectrum emphasizes the extensive mid-UV and near-UV absorption exhibited by the REC_{20} cluster, especially the excellent performance exhibited by the PmC_{20} cluster. These findings suggest that their absorption properties in the UV and visible spectrum can be exploited for promising applications in solar energy converters or ultra-high-sensitivity near-UV photodetectors.

4. CONCLUSION

The structures of a series of minimally EMFs encapsulating rare earth atoms REC_{20} clusters (RE = Sc, Y, La, Ce, Pr, Nd, Pm, Sm, Eu, Gd) have been optimized using DFT. RE atoms are always located in the center of the C_{20} cage. The high-stability superatoms of REC_{20} clusters (RE = Pr, Nd, Pm, Sm) originate from the widening of the HOMO−LUMO gap caused by the larger contribution of the RE atom's 4f electron orbital to the cluster frontier orbital. NPA and spin density analyses indicate that the 4f orbital of RE atoms contributes significantly to the total magnetic moment. The tunable magnetic moment of REC_{20} clusters increases monotonically from 0 to 6 μ_B. ICSSzz isosurfaces and GIMIC show that the aromaticity of the REC_{20} clusters gradually strengthens with the increase in 4f electrons in RE atoms. The diamagnetic current area in the cage expands from the central atom to the C_{20} cage, indicating that the delocalized electron distribution area in the cage becomes larger. The UV−vis spectrum of REC_{20} clusters shows strong absorption in the mid-UV and near-UV bands. In summary, REC_{20} clusters encapsulating lanthanide metal atoms show potential as stable, highly magnetic assembly materials and as ultrahighly sensitive near-UV photodetection materials.

■ ASSOCIATED CONTENT

Supporting Information

The Supporting Information is available free of charge at https://pubs.acs.org/doi/10.1021/acsomega.4c05912.

Tables of Cartesian coordinates for REC_{20} clusters optimized at the PBE0/RE/SDD//C/cc-pVTZ level; relative energies of REC_{20} clusters with different spin multiplicities at the PBE0/RE/SDD//C/cc-pVTZ level; Figures of structures of REC_{20} clusters optimized at the PBE0/RE/SDD//C/cc-pVTZ level; HOMO−LUMO gaps in conjunction with corresponding orbitals of REC_{20} obtained at the PBE0/RE/SDD//C/cc-pVTZ level; HOMO−LUMO gaps in conjunction with corresponding orbitals of REC_{20} obtained at the PBE0/RE/SDD//C/cc-pVTZ level; molecular orbitals of REC_{20} clusters; bonding analyses of AdNDP orbitals of REC_{20} (PDF)

Three-dimensional dynamic visual representation of the magnetically induced current (MP4)

Three-dimensional dynamic visual representation of the magnetically induced current (MP4)

Three-dimensional dynamic visual representation of the magnetically induced current (MP4)

Three-dimensional dynamic visual representation of the magnetically induced current (MP4)

■ AUTHOR INFORMATION

Corresponding Authors

Huai-Qian Wang − *College of Information Science and Engineering, Huaqiao University, Xiamen 361021, China; College of Engineering, Huaqiao University, Quanzhou 362021, China;* orcid.org/0000-0003-0388-510X; Email: hqwang@hqu.edu.cn

Hui-Fang Li − *College of Engineering, Huaqiao University, Quanzhou 362021, China*; Email: hfli@hqu.edu.cn

Authors

Jia-Ming Zhang − *College of Information Science and Engineering, Huaqiao University, Xiamen 361021, China*

Xun-Jie Mei − *College of Engineering, Huaqiao University, Quanzhou 362021, China*

Yong-Hang Zhang − *College of Information Science and Engineering, Huaqiao University, Xiamen 361021, China*

Hao Zheng − *College of Information Science and Engineering, Huaqiao University, Xiamen 361021, China*

Complete contact information is available at: https://pubs.acs.org/10.1021/acsomega.4c05912

Notes

The authors declare no competing financial interest.

■ ACKNOWLEDGMENTS

The project was supported by the Natural Science Foundation of Fujian Province of China (Grant No. 2023J01141), the Natural Science Foundation of Xiamen (Grant No. 3502Z202373051), the Science and Technology Plan of Quanzhou (Grant Nos. 2018C077R and 2018C078R), and the New Century Excellent Talents in Fujian Province University (Grant No. 2014FJ-NCET-ZR07).

■ REFERENCES

(1) Taninaka, A.; Ochiai, T.; Kanazawa, K.; Takeuchi, O.; Shigekawa, H. Probing of electronic structures of La@C_{82} superatoms upon clustering realized using glycine nanocavities. *Appl. Phys. Express* **2015**, *8* (12), 125503.

(2) Xie, W. Y.; Zhu, Y.; Wang, J. P.; Cheng, A. H.; Wang, Z. G. Magnetic coupling induced self-assembly at atomic level*. *Chin. Phys. Lett.* **2019**, *36* (11), 116401.

(3) Xie, W. Y.; Yu, F. M.; Wu, X. C.; Liu, Z. H.; Yan, Q.; Wang, Z. G. Constructing the bonding interactions between endohedral metallofullerene superatoms by embedded atomic regulation. *Phys. Chem. Chem. Phys.* **2021**, *23* (30), 15899−15903.

(4) Shen, Y. B.; Cui, M. X.; Takaishi, S.; Kawasoko, H.; Sugimoto, K.; Tsumuraya, T.; Otsuka, A.; Kwon, E.; Yoshida, T.; Hoshino, N.; Kawachi, K.; Kasama, Y.; Akutagawa, T.; Fukumura, T.; Yamashita, M. Heterospin frustration in a metal-fullerene-bonded semiconductive antiferromagnet. *Nat. Commun.* **2022**, *13* (1), 495.

(5) Wang, R.; Yang, X. R.; Huang, W. R.; Liu, Z. H.; Zhu, Y.; Liu, H. Y.; Wang, Z. G. Superatomic states under high pressure. *iScience* **2023**, *26* (4), 106281.
(6) Heath, J. R.; O'Brien, S. C.; Zhang, Q.; Liu, Y.; Curl, R. F.; Tittel, F. K.; Smalley, R. E. Lanthanum complexes of spheroidal carbon shells. *J. Am. Chem. Soc.* **1985**, *107* (25), 7779−7780.
(7) Ito, Y.; Fujita, W.; Okazaki, T.; Sugai, T.; Awaga, K.; Nishibori, E.; Takata, M.; Sakata, M.; Shinohara, H. Magnetic properties and crystal structure of solvent-free Sc@C_{82} metallofullerene microcrystals. *ChemPhysChem* **2007**, *8* (7), 1019−1024.
(8) Zuo, T. M.; Olmstead, M. M.; Beavers, C. M.; Balch, A. L.; Wang, G. B.; Yee, G. T.; Shu, C. Y.; Xu, L. S.; Elliott, B.; Echegoyen, L.; Duchamp, J. C.; Dorn, H. C. Preparation and structural characterization of the I_h and the D_{5h} isomers of the endohedral fullerenes $Tm_3N@C_{80}$: icosahedral C_{80} Cage encapsulation of a trimetallic nitride magnetic cluster with three uncoupled Tm^{3+} ions. *Inorg. Chem.* **2008**, *47* (12), 5234−5244.
(9) Aoyagi, S.; Nishibori, E.; Sawa, H.; Sugimoto, K.; Takata, M.; Miyata, Y.; Kitaura, R.; Shinohara, H.; Okada, H.; Sakai, T.; Ono, Y.; Kawachi, K.; Yokoo, K.; Ono, S.; Omote, K.; Kasama, Y.; Ishikawa, S.; Komuro, T.; Tobita, H. A layered ionic crystal of polar Li@C_{60} superatoms. *Nat. Chem.* **2010**, *2* (8), 678−683.
(10) Popov, A. A.; Chen, C.; Yang, S.; Lipps, F.; Dunsch, L. Spin-flow vibrational spectroscopy of molecules with flexible spin density: electrochemistry, ESR, cluster and spin dynamics, and bonding in $TiSc_2N@C_{80}$. *ACS Nano* **2010**, *4* (8), 4857−4871.
(11) Zaka, M.; Warner, J. H.; Ito, Y.; Morton, J. J. L.; Rümmeli, M. H.; Pichler, T.; Ardavan, A.; Shinohara, H.; Briggs, G. A. D. Exchange interactions of spin-active metallofullerenes in solid-state carbon networks. *Phys. Rev. B* **2010**, *81* (7), 075424.
(12) Zhao, J. J.; Huang, X. M.; Jin, P.; Chen, Z. F. Magnetic properties of atomic clusters and endohedral metallofullerenes. *Coord. Chem. Rev.* **2015**, *289−290*, 315−340.
(13) Yang, S. F.; Wei, T.; Jin, F. When metal clusters meet carbon cages: endohedral clusterfullerenes. *Chem. Soc. Rev.* **2017**, *46* (16), 5005−5058.
(14) Bologna, F.; Mattioli, E. J.; Bottoni, A.; Zerbetto, F.; Calvaresi, M. Interactions between endohedral metallofullerenes and proteins: The Gd@C_{60}-Lysozyme model. *ACS Omega* **2018**, *3* (10), 13782−13789.
(15) Mwakisege, J. G.; Schweitzer, G.; Mirzadeh, S. Synthesis and stability of actinium-225 endohedral fullerenes, ^{225}Ac@C_{60}. *ACS Omega* **2020**, *5* (42), 27016−27025.
(16) Zhao, J. J.; Du, Q. Y.; Zhou, S.; Kumar, V. Endohedrally doped cage clusters. *Chem. Rev.* **2020**, *120* (17), 9021−9163.
(17) Zhang, W. X.; Li, M. Y.; He, J.; Zhao, X. Theoretical Insights into the Metal-Nonmetal Interaction Inside $M_2O@C_{2V}(31922)$-C_{80} (M = Sc or Gd). *ACS Omega* **2022**, *7* (47), 42883−42889.
(18) Ismael, A. K. 20-State molecular switch in a Li@C_{60} complex. *ACS Omega* **2023**, *8* (22), 19767−19771.
(19) Sarfaraz, S.; Yar, M.; Hussain, A.; Lakhani, A.; Gulzar, A.; Ans, M.; Rashid, U.; Hussain, M.; Muhammad, S.; Bayach, I.; Sheikh, N. S.; Ayub, K. Metallofullerenes as robust single-atom catalysts for adsorption and dissociation of hydrogen molecules: A density functional study. *ACS Omega* **2023**, *8* (39), 36493−36505.
(20) Lu, X.; Chen, Z. F. Curved Pi-conjugation, aromaticity, and the related chemistry of small fullerenes (<C_{60}) and single-walled carbon nanotubes. *Chem. Rev.* **2005**, *105* (10), 3643−3696.
(21) Handschuh, H.; Ganteför, G.; Kessler, B.; Bechthold, P. S.; Eberhardt, W. Stable configurations of carbon clusters: chains, rings, and fullerenes. *Phys. Rev. Lett.* **1995**, *74* (7), 1095−1098.
(22) Martin, J. M. L. C_{28}: the smallest stable fullerene? *Chem. Phys. Lett.* **1996**, *255* (1), 1−6.
(23) Guo, T.; Diener, M. D.; Chai, Y.; Alford, M. J.; Haufler, R. E.; McClure, S. M.; Ohno, T.; Weaver, J. H.; Scuseria, G. E.; Smalley, R. E. Uranium stabilization of C_{28}: a tetravalent fullerene. *Science* **1992**, *257* (5077), 1661−1664.
(24) Zhao, K.; Pitzer, R. M. Electronic structure of C_{28}, Pa@C_{28}, and U@C_{28}. *J. Phys. Chem.* **1996**, *100* (12), 4798−4802.
(25) Makurin, Y. N.; Sofronov, A. A.; Gusev, A. I.; Ivanovsky, A. L. Electronic structure and chemical stabilization of C_{28} fullerene. *Chem. Phys.* **2001**, *270* (2), 293−308.
(26) Peng, S.; Zhang, Y.; Li, X. J.; Ren, Y.; Zhang, D. X. DFT calculations on the structural stability and infrared spectroscopy of endohedral metallofullerenes. *Spectrochim. Acta, Part A* **2009**, *74* (2), 553−557.
(27) Zhang, Y.; Peng, S.; Li, X. J.; Zhang, D. X. Structural stability, electronegativity and electronic property of endohedral TM@C_{24} and exohedral TMC_{24} (TM = Sc, Y and La) metallofullerene complexes: Density-functional theory investigations. *J. Mol. Struct. THEOCHEM* **2010**, *947* (1), 16−21.
(28) Dunk, P. W.; Kaiser, N. K.; Mulet-Gas, M.; Rodríguez-Fortea, A.; Poblet, J. M.; Shinohara, H.; Hendrickson, C. L.; Marshall, A. G.; Kroto, H. W. The smallest stable fullerene, M@C_{28} (M = Ti, Zr, U): stabilization and growth from carbon vapor. *J. Am. Chem. Soc.* **2012**, *134* (22), 9380−9389.
(29) Manna, D.; Ghanty, T. K. Prediction of a new series of thermodynamically stable actinide encapsulated fullerene systems fulfilling the 32-electron Pprinciple. *J. Phys. Chem. C* **2012**, *116* (48), 25630−25641.
(30) Ryzhkov, M. V.; Ivanovskii, A. L.; Delley, B. Electronic structure of endohedral fullerenes An@C_{28} (An = Th - Md). *Comput. Theor. Chem.* **2012**, *985*, 46−52.
(31) Manna, D.; Sirohiwal, A.; Ghanty, T. K. Pu@C_{24}: a new example satisfying the 32-electron principle. *J. Phys. Chem. C* **2014**, *118* (13), 7211−7221.
(32) Miralrio, A.; Sansores, L. E. On the search of stable, aromatic and ionic endohedral compounds of C_{28}: A theoretical study. *Comput. Theor. Chem.* **2016**, *1083*, 53−63.
(33) Muñoz-Castro, A.; Bruce King, R. Evaluation of bonding, electron affinity, and optical properties of M@C_{28} (M = Zr, Hf, Th, and U): Role of d- and f-orbitals in endohedral fullerenes from relativistic DFT calculations. *J. Comput. Chem.* **2017**, *38* (1), 44−50.
(34) Dai, X.; Gao, Y.; Jiang, W.; Lei, Y.; Wang, Z. U@C28: the electronic structure induced by the 32-electron principle. *Phys. Chem. Chem. Phys.* **2015**, *17* (36), 23308−23311.
(35) Dognon, J.-P.; Clavaguéra, C.; Pyykkö, P. A Predicted Organometallic Series Following a 32-Electron Principle: An@C_{28} (An = Th, Pa^+, U^{2+}, Pu^{4+}). *J. Am. Chem. Soc.* **2009**, *131* (1), 238−243.
(36) ErkoÇ, Ş. Metal atom endohedrally doped C_{20} cage structure: (X@C_{20}; X = Ni, Fe, Co). *Int. J. Mod. Phys. C* **2005**, *16* (10), 1553−1560.
(37) An, Y. P.; Yang, C. L.; Wang, M. S.; Ma, X. G.; Wang, D. H. Ab initio investigations of the charge transport properties of endohedral M@C_{20} (M = Na and K) metallofullerenes. *Chin. Phys. B* **2010**, *19* (11), 113402.
(38) Nikolai, A. P.; Eugene, F. K.; Sergey, A. V.; Nguyen Ngoc, H.; Oleg, N. B.; Andrei, I. S.; Irina, V. L.; Andrey, A. K.; Andrey, M. P.; Yurii, E. L. Magnetically operated nanorelay based on two single-walled carbon nanotubes filled with endofullerenes Fe@C_{20}. *J. Nanophotonics* **2010**, *4* (1), 041675.
(39) Samah, M.; Boughiden, B. Structures, electronic and magnetic properties of C_{20} fullerenes doped transition metal atoms M@C_{20} (M = Fe, Co, Ti, V). *Int. J. Mod. Phys. C* **2010**, *21* (12), 1469−1477.
(40) An, Y. P.; Yang, C. L.; Wang, M. S.; Ma, X. G.; Wang, D. H. Geometrical and electronic properties of the clusters of C_{20} cage doped with alkali metal atoms. *J. Cluster Sci.* **2011**, *22* (1), 31−39.
(41) Wu, J. L.; Sun, Z. C.; Li, X. J.; Ma, B.; Tian, M. S.; Li, S. R. Theoretical study on the smallest endohedral metallofullerenes: TM@C_{20} (TM = Ce and Gd). *Int. J. Quantum Chem.* **2011**, *111* (14), 3786−3792.
(42) Manna, D.; Ghanty, T. K. Theoretical prediction of icosahedral U@C_{20} and analogous systems with high HOMO-LUMO Gap. *J. Phys. Chem. C* **2012**, *116* (31), 16716−16725.
(43) Baei, M. T.; Soltani, A.; Torabi, P.; Hosseini, F. Formation and electronic structure of C_{20} fullerene transition metal clusters. *Monatsh. Chem.* **2014**, *145* (9), 1401−1405.

https://doi.org/10.1021/acsomega.4c05912
ACS Omega 2024, 9, 35197−35208

(44) Meng, F. C.; Zhou, Z. W.; Zhang, P. L.; Jiang, M.; Xu, X. L.; Wang, Y.; Gou, J. H.; Hui, D.; Die, D. Encapsulation of an f-block metal atom/ion to enhance the stability of C_{20} with the I_h symmetry. *Phys. Chem. Chem. Phys.* **2015**, *17* (6), 4328−4336.
(45) Gonzalez, M.; Lujan, S.; Beran, K. A. Investigation into the molecular structure, electronic properties, and energetic stability of endohedral (TM@C_{20}) and exohedral (TM-C_{20}) metallofullerene derivatives of C_{20}: TM = Group 11 and 12 transition metal atoms/ions. *Comput. Theor. Chem.* **2017**, *1119*, 32−44.
(46) Muñoz-Castro, A.; King, R. B. On the formation of smaller p-block endohedral fullerenes: Bonding analysis in the E@C_{20} (E = Si, Ge, Sn, Pb) series from relativistic DFT calculations. *J. Comput. Chem.* **2017**, *38* (19), 1661−1667.
(47) Li, J. R.; Wang, R.; Huang, W. R.; Zhu, Y.; Teo, B. K.; Wang, Z. G. Smallest Endohedral Metallofullerenes $[Mg@C_{20}]^n$ (n = 4, 2, 0, −2, and −4): Endo-Ionic Interaction in Superatoms. *J. Phys. Chem. Lett.* **2023**, *14* (11), 2862−2868.
(48) Adamo, C.; Barone, V. Toward reliable density functional methods without adjustable parameters: The PBE0 model. *J. Chem. Phys.* **1999**, *110* (13), 6158−6170.
(49) Xie, B.; Wang, H. Q.; Li, H. F.; Zhang, J. M.; Zeng, J. K.; Qin, L. X.; Mei, X. J. Structural and electronic properties of bimetallic Eu_2 doped silicon-based clusters. *J. Cluster Sci.* **2024**, *35* (1), 115−127.
(50) Xie, B.; Wang, H. Q.; Li, H.-F.; Zhang, J. M.; Zeng, J. K.; Mei, X. J.; Zhang, Y. H.; Zheng, H.; Qin, L. X. Making sense of the growth behavior of ultra-high magnetic Gd_2-doped silicon clusters. *Molecules* **2023**, *28* (13), 5071.
(51) Zeng, J. K.; Wang, H. Q.; Li, H. F.; Zheng, H.; Zhang, J. M.; Mei, X. J.; Zhang, Y. H.; Ding, X. L. Exploring the stability and aromaticity of rare earth doped tin cluster MSn_{16}^- (M = Sc, Y, La). *Phys. Chem. Chem. Phys.* **2024**, *26* (4), 2986−2994.
(52) Dolg, M.; Wedig, U.; Stoll, H.; Preuss, H. Energy-adjusted ab initio pseudopotentials for the first row transition elements. *J. Chem. Phys.* **1987**, *86* (2), 866−872.
(53) Andrae, D.; Häußermann, U.; Dolg, M.; Stoll, H.; Preuß, H. Energy-adjustedab initio pseudopotentials for the second and third row transition elements. *Theor. Chim. Acta* **1990**, *77* (2), 123−141.
(54) Dolg, M.; Stoll, H.; Savin, A.; Preuss, H. Energy-adjusted pseudopotentials for the rare earth elements. *Theor. Chim. Acta* **1989**, *75* (3), 173−194.
(55) Dolg, M.; Stoll, H.; Preuss, H. A combination of quasirelativistic pseudopotential and ligand field calculations for lanthanoid compounds. *Theor. Chim. Acta* **1993**, *85* (6), 441−450.
(56) Hehre, W. J.; Ditchfield, R.; Pople, J. A. Self-consistent molecular orbital methods. XII. Further extensions of Gaussian-type basis sets for use in molecular orbital studies of organic molecules. *J. Chem. Phys.* **1972**, *56* (5), 2257−2261.
(57) Hariharan, P. C.; Pople, J. A. The influence of polarization functions on molecular orbital hydrogenation energies. *Theor. Chim. Acta* **1973**, *28* (3), 213−222.
(58) Dunning, T. H., Jr Gaussian basis sets for use in correlated molecular calculations. I. The atoms boron through neon and hydrogen. *J. Chem. Phys.* **1989**, *90* (2), 1007−1023.
(59) Dolg, M.; Stoll, H.; Preuss, H. Energy-adjusted ab initio pseudopotentials for the rare earth elements. *J. Chem. Phys.* **1989**, *90* (3), 1730−1734.
(60) Frisch, M. J.; Trucks, G. W.; Schlegel, H. B.; Scuseria, G. E.; Robb, M. A.; Cheeseman, J. R.; Scalmani, G.; Barone, V.; Mennucci, B.; Petersson, G. A.; Nakatsuji, H.; Caricato, M.; Li, X.; Hratchian, H. P.; Izmaylov, A. F.; Bloino, J.; Zheng, G.; Sonnenberg, J. L.; Hada, M.; Ehara, M.; Toyota, K.; Fukuda, R.; Hasegawa, J.; Ishida, M.; Nakajima, T.; Honda, Y.; Kitao, O.; Nakai, H.; Vreven, T.; Montgomery, J. A., Jr; Peralta, J. E.; Ogliaro, F.; Bearpark, M.; Heyd, J. J.; Brothers, E.; Kudin, K. N.; Staroverov, V. N.; Keith, T.; Kobayashi, R.; Normand, J.; Raghavachari, K.; Rendell, A.; Burant, J. C.; Iyengar, S. S.; Tomasi, J.; Cossi, M.; Rega, N.; et al. *Gaussian09*; Gaussian Inc.: Wallingford, CT, USA, 2010.
(61) Schleyer, P. v. R.; Maerker, C.; Dransfeld, A.; Jiao, H.; van Eikema Hommes, N. J. R. Nucleus-independent chemical shifts: a simple and efficient aromaticity probe. *J. Am. Chem. Soc.* **1996**, *118* (26), 6317−6318.
(62) Klod, S.; Kleinpeter, E. Ab initio calculation of the anisotropy effect of multiple bonds and the ring current effect of arenes—application in conformational and configurational analysis. *J. Chem. Soc., Perkin Trans. 2* **2001**, No. 10, 1893−1898.
(63) Wang, X.; Liu, Z. Y.; Yan, X. F.; Lu, T.; Zheng, W. L.; Xiong, W. W. Bonding character, electron delocalization, and aromaticity of cyclo[18]carbon (C_{18}) precursors, C_{18}-$(CO)_n$ (n = 6, 4, and 2): focusing on the effect of carbonyl (-CO) groups. *Chem.—Eur. J.* **2022**, *28* (7), No. e202103815.
(64) Lu, T.; Chen, F. Multiwfn: A multifunctional wavefunction analyzer. *J. Comput. Chem.* **2012**, *33* (5), 580−592.
(65) Humphrey, W.; Dalke, A.; Schulten, K. VMD: Visual molecular dynamics. *J. Mol. Graphics* **1996**, *14* (1), 33−38.
(66) Breneman, C. M.; Wiberg, K. B. Determining atom-centered monopoles from molecular electrostatic potentials. The need for high sampling density in formamide conformational analysis. *J. Comput. Chem.* **1990**, *11* (3), 361−373.
(67) Jusélius, J.; Sundholm, D.; Gauss, J. Calculation of current densities using gauge-including atomic orbitals. *J. Chem. Phys.* **2004**, *121* (9), 3952−3963.
(68) An, W.; Gao, Y.; Bulusu, S.; Zeng, X. C. Ab initio calculation of bowl, cage, and ring isomers of C_{20} and C_{20}^-. *J. Chem. Phys.* **2005**, *122* (20), 204109.
(69) Parr, R. G.; Pearson, R. G. Absolute hardness: companion parameter to absolute electronegativity. *J. Am. Chem. Soc.* **1983**, *105* (26), 7512−7516.
(70) Manolopoulos, D. E.; May, J. C.; Down, S. E. Theoretical studies of the fullerenes: C34 to C70. *Chem. Phys. Lett.* **1991**, *181* (2), 105−111.
(71) Parr, R. G.; Zhou, Z. Absolute hardness: unifying concept for identifying shells and subshells in nuclei, atoms, molecules, and metallic clusters. *Acc. Chem. Res.* **1993**, *26* (5), 256−258.
(72) de Heer, W. A. The physics of simple metal clusters: experimental aspects and simple models. *Rev. Mod. Phys.* **1993**, *65* (3), 611−676.
(73) Hirsch, A.; Chen, Z.; Jiao, H. Spherical aromaticity in I_h symmetrical fullerenes: the $2(N+1)^2$ rule. *Angew. Chem., Int. Ed.* **2000**, *39* (21), 3915−3917.
(74) Reed, A. E.; Weinstock, R. B.; Weinhold, F. Natural population analysis. *J. Chem. Phys.* **1985**, *83* (2), 735−746.
(75) Lu, T.; Chen, F. W. Atomic dipole moment corrected Hirshfeld population method. *J. Theor. Comput. Chem.* **2012**, *11* (01), 163−183.
(76) Lu, T.; Chen, F. W. Comparison of computational methods for atomic charges. *Acta Phys. Chim. Sin.* **2012**, *28* (01), 1−18.
(77) Zubarev, D. Y.; Boldyrev, A. I. "Developing paradigms of chemical bonding: adaptive natural density partitioning. *Phys. Chem. Chem. Phys.* **2008**, *10* (34), 5207−5217.
(78) Zdetsis, A. D. Open-shell magnetic states in alternant and non-alternant nanographenes: Conceptions and misconceptions. *Carbon Trends* **2024**, *14*, 100330.
(79) Wang, X.; Liu, Z. Y.; Wang, J. J.; Lu, T.; Xiong, W. W.; Yan, X. F.; Zhao, M. D.; Orozco-Ic, M. Electronic structure and aromaticity of an unusual cyclo[18]carbon precursor, $C_{18}Br_6$. *Chem.—Eur. J.* **2023**, *29* (31), No. e202300348.
(80) Zdetsis, A. D. Structural, cohesive, electronic, and aromatic properties of selected fully and partially hydrogenated carbon fullerenes. *J. Phys. Chem. C* **2011**, *115* (30), 14507−14516.
(81) Fliegl, H.; Taubert, S.; Lehtonen, O.; Sundholm, D. The gauge including magnetically induced current method. *Phys. Chem. Chem. Phys.* **2011**, *13* (46), 20500−20518.

https://doi.org/10.1021/acsomega.4c05912
ACS Omega 2024, 9, 35197−35208